

Towards the discovery of high critical magnetic field superconductors

Benjamin Geisler,^{1,2,*} Philip M. Dee,³ James J. Hamlin,¹ Gregory R. Stewart,¹ Richard G. Hennig,^{2,4} and P.J. Hirschfeld¹

¹*Department of Physics, University of Florida, Gainesville, Florida 32611, USA*

²*Department of Materials Science and Engineering, University of Florida, Gainesville, Florida 32611, USA*

³*Computational Sciences and Engineering Division,*

Oak Ridge National Laboratory, Oak Ridge, Tennessee, 37831-6494, USA

⁴*Quantum Theory Project, University of Florida, Gainesville, Florida 32611, USA*

(Dated: January 30, 2026)

Superconducting materials are of significant technological relevance for a broad range of applications, and intense research efforts aim at enhancing the critical temperature T_c . Intriguingly, while numerous studies have explored different computational and machine-learning routes to predict T_c , the fundamental role of the critical magnetic field has so far been overlooked. Here we open a new frontier in superconductor discovery by presenting a consistent computational database of critical fields H_c , H_{c1} , and H_{c2} for over 7,300 electron-phonon-paired superconductors covering distinct materials classes. A theoretical framework is developed that combines $\alpha^2 F(\omega)$ spectral functions and highly accurate Fermi surfaces from density functional theory with clean-limit Eliashberg theory to obtain the coherence lengths, London penetration depths, and Ginzburg-Landau parameters. We discover an unexpectedly large number of Type-I superconductors and show that larger unit cells generically support higher critical fields and Type-II behavior. We identify the importance of going beyond BCS theory by including strong-coupling corrections to the superconducting gap and electron-phonon renormalizations of the effective mass for predictions of critical fields across materials. These results provide a framework for foundational AI models that realize the concept of inverse materials design for high- T_c and high-critical-field superconductors.

I. INTRODUCTION

The technological relevance of superconducting materials has driven substantial efforts to identify next-generation compounds with enhanced critical temperature T_c [1–13]. A successful route towards this goal is the combination of computational and theoretical methods for materials discovery. This strategy has led to notable breakthroughs, most prominently the prediction and subsequent experimental confirmation of high- T_c hydride superconductors under pressure [14–18]. The recent rise of machine learning has considerably accelerated these explorations [19–29], a necessity in light of the immense search space for superconductor discovery. However, superconductivity as a macroscopic quantum many-body phenomenon remains extremely challenging to predict.

It has become increasingly clear that T_c alone is not the decisive metric of technological usefulness. Critical magnetic fields and the associated critical currents also play a central role, as do mechanical aspects such as ductility and processability [30]. For example, high- T_c cuprates are limited by their layered structure and resulting two-dimensional superconductivity, which facilitate vortex-liquid formation [31]. Similarly, MgB₂, one of the highest- T_c conventional superconductors, faces manufacturing challenges and exhibits a two-gap superconducting structure that, while being a feature of strong scientific interest [32, 33], further limits practical applications compared to e.g. Nb-based compounds.

Interestingly, the technological importance of critical magnetic fields has been largely overlooked: High critical fields are essential for many key applications, including high-

performance magnets for high-field laboratories, fusion reactors, particle accelerators, and MRI machines.

These considerations require a paradigm shift in the field. The primary goal is to avoid the need for helium-based cooling, as the cost of cryogenic operation increases by orders of magnitude as T_c decreases. Thus, we underline the following three primary requirements for a practical superconductor: (i) T_c sufficiently high to allow a safe operating temperature well above liquid helium, e.g., $\gtrsim 20$ K; (ii) Critical fields to achieve required critical currents and resulting magnetic fields for applications, e.g., $\gtrsim 10$ T [34]; (iii) Ductility and processability to enable wire fabrication. Hence, rather than focusing solely on high T_c , it is imperative to systematically identify superconductors with large critical fields.

Here we take a first step in this new direction by establishing a first-principles workflow to predict thermodynamic critical fields H_c , lower critical fields H_{c1} , and upper critical fields H_{c2} that combines clean-limit Eliashberg theory with $\alpha^2 F(\omega)$ spectral functions and Fermi surface properties from density functional theory. We construct a comprehensive database for more than 7,300 electron-phonon-paired superconductors spanning diverse materials classes. Using this unique perspective, we identify compounds with high critical fields and uncover surprising trends that challenge prevailing wisdom in the field. In particular, we find an unexpectedly large number of Type-I superconductors and show that higher critical fields and Type-II behavior are favored in materials with larger unit cells. We further demonstrate the necessity of going beyond BCS theory to achieve reliable predictions of critical fields. These results lay the groundwork for future foundational AI models enabling inverse materials design of high- T_c and high-critical-field superconductors.

* benjamin.geisler@ufl.edu

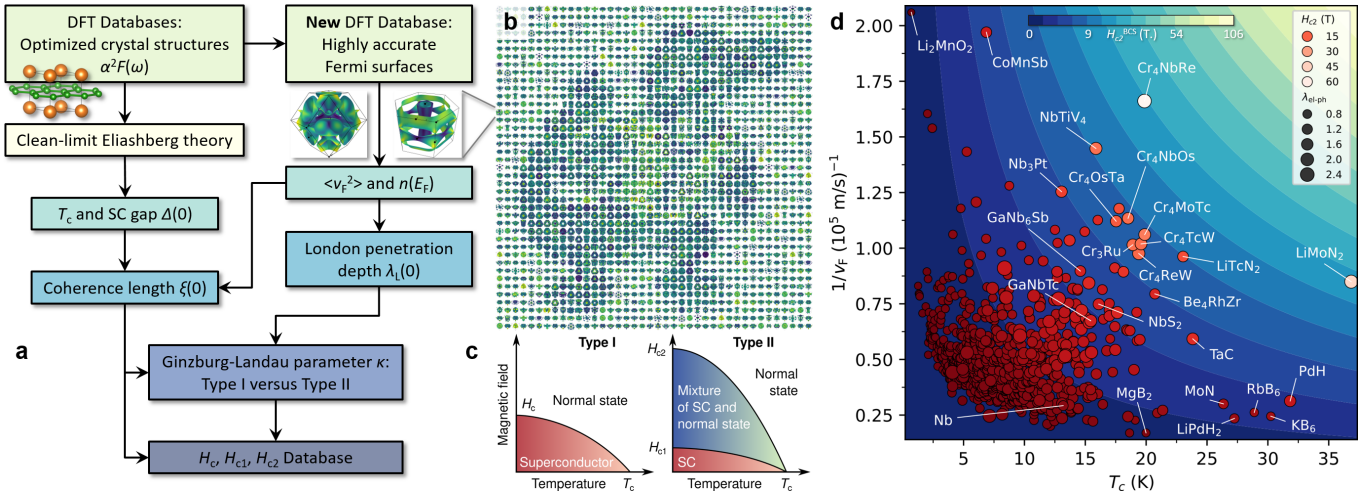


Figure 1. First-principles database of superconducting critical magnetic fields. **a** The workflow developed here to obtain a consistent database of critical fields and related superconducting properties entirely from first principles. **b** The fundamental ingredient is a new database of Fermi surfaces, colored here by the Fermi velocities; a selection has been compiled in the form of a mosaic where each pixel is a Fermi surface. **c** Explanation of the different critical fields. **d** Upper critical fields at zero temperature for all Type-II superconductors in our database, systematically ranked in a $(T_c, 1/v_F)$ scatterplot. The blue-yellow background shows H_{c2}^{BCS} to structure the data, as described in the text. The point colors reflect the actual upper critical fields $H_{c2} > H_{c2}^{\text{BCS}}$ determined by using the calculated Eliashberg gaps, which include strong-coupling corrections, and considering effective-mass renormalizations of the Fermi velocities due to electron-phonon interactions $\lambda_{\text{el-ph}}$.

II. RESULTS

A. Workflow: First-principles database of superconducting critical magnetic fields

We construct a database of superconducting critical fields for $\sim 7,300$ realistic materials by combining density functional theory (DFT) [35] and clean-limit Eliashberg theory [36, 37]. All quantities are obtained consistently from first principles, using a workflow we developed and describe below [Fig. 1(a)]. Importantly, our philosophy here is to present and discuss a broad set of materials, prioritizing comprehensive coverage. Therefore, we deliberately avoid excluding any compounds based on physical intuition, and retain all materials in the final results, including outliers.

We start from two established databases of electron-phonon superconductors that provide DFT-optimized crystal structures and corresponding calculated $\alpha^2 F(\omega)$ Eliashberg spectral functions [Fig. 1(a)], from our group [27] and from Cerqueira *et al.* [38], complemented by new calculations for this work. These parent databases cover a wide variety of materials across the periodic table.

By solving the isotropic Eliashberg equations [39, 40] in a high-throughput framework, we explicitly calculate the superconducting critical temperature T_c and the superconducting gap at zero temperature $\Delta(0)$ for the reference isotropic system, explicitly accounting for strong-coupling corrections. In parallel, we perform high-throughput DFT calculations [41–43] to obtain accurate Fermi surfaces for all materials [Fig. 1(b)]. Subsequently, we calculate a key ingredient, the

averaged Fermi velocities:

$$\langle v_F^2 \rangle = \frac{1}{A_{\text{FS}} \hbar^2} \int_{\text{FS}} dn \left(\nabla_{\vec{k}} \varepsilon(\vec{k}) \right)^2 = \langle v_x^2 \rangle + \langle v_y^2 \rangle + \langle v_z^2 \rangle. \quad (1)$$

Our methodology provides the sheet- and direction-resolved components of the squared velocity operator (i.e., the anisotropic information). Here, we use the isotropic average, integrated over the entire Fermi surface. The DFT high-throughput sampling also provides accurate total densities of states $n(E_F)$ by using the tetrahedron method, which we normalize by the unit cell volume. Further numerical details are reported in the Methods section.

From these fundamental quantities, we calculate the superconducting coherence length,

$$\xi(0) = \frac{\hbar \sqrt{\langle v_F^2 \rangle}}{\pi \langle \Delta(0) \rangle}, \quad (2)$$

and the London penetration depth,

$$\lambda_L(0) = \sqrt{\frac{m}{\mu_0 n_s e^2}}, \quad (3)$$

where $\langle \Delta(0) \rangle$ is an appropriately averaged gap function over the Fermi surface [44], which we replace by $\Delta(0)$ in the absence of information on the anisotropy of the pairing interaction. The expressions given apply formally to single-band systems in the BCS clean limit as $T \rightarrow 0$ [45]. While Eq. (3) is often used to infer the superfluid density n_s from a measured λ_L , here we recast it into a form in which all quantities are obtained consistently from DFT:

$$\lambda_L(0) = \sqrt{\frac{3}{\mu_0 e^2 n(E_F) \langle v_F^2 \rangle}}, \quad (4)$$

by substituting the effective mass and superfluid density with the volume-normalized total density of states and averaged isotropic Fermi velocity. Experimentally, the measured superconducting penetration depths are always larger than the BCS $\lambda_L(0)$ [45].

The BCS expressions for ξ and λ_L are renormalized within the more complete Eliashberg theory of superconductivity by the electron-phonon coupling strength,

$$\lambda_{\text{el-ph}} = 2 \int d\omega \alpha^2 F(\omega)/\omega \quad (5)$$

via the factors

$$\lambda_L \rightarrow \lambda_L \sqrt{1 + \lambda_{\text{el-ph}}}, \quad \xi \rightarrow \xi/(1 + \lambda_{\text{el-ph}}), \quad (6)$$

which follows from

$$n(E_F) \rightarrow n(E_F)(1 + \lambda_{\text{el-ph}}), \quad v_F \rightarrow v_F/(1 + \lambda_{\text{el-ph}}), \quad (7)$$

accounting for the effective-mass dressing of the electron by its interaction with the phonon system. We find that these renormalizations lead to substantial modifications of the Ginzburg-Landau parameter κ and the corresponding critical fields, as detailed below.

The Ginzburg-Landau parameter, defined as

$$\kappa = \lambda_L/\xi, \quad (8)$$

allows us to fundamentally distinguish between Type-I ($\kappa < 1/\sqrt{2}$) and Type-II superconductors ($\kappa > 1/\sqrt{2}$).

The upper critical field of Type-II superconductors at zero temperature is given by

$$H_{c2} = \frac{\Phi_0}{2\pi\xi^2} = \frac{\pi^2}{2e\hbar} \frac{\Delta^2}{\langle v_F^2 \rangle}, \quad (9)$$

and depends essentially on the superconducting gap and the averaged Fermi velocity, with the superconducting flux quantum $\Phi_0 = h/2e$.

For the lower critical field of Type-II superconductors, we employ the expression proposed by Brandt [46]:

$$H_{c1} = \frac{\Phi_0}{4\pi} \frac{\ln(\kappa) + \alpha(\kappa)}{\lambda_L^2} = H_{c2} \frac{\ln(\kappa) + \alpha(\kappa)}{2\kappa^2}, \quad (10)$$

where $\alpha(\kappa)$ has been determined numerically. Interestingly, the right-hand side shows that H_{c1} can be expressed in terms of H_{c2} multiplied by a κ -dependent factor.

The thermodynamic critical field of Type-I superconductors follows from the Ginzburg-Landau expression:

$$H_c = \frac{\Phi_0}{2\sqrt{2}\pi} \frac{1}{\lambda_L \xi} = H_{c2} \frac{1}{\sqrt{2}\kappa}. \quad (11)$$

Again, H_c can be expressed in terms of (a hypothetical) H_{c2} divided by $\sqrt{2}\kappa$. These equations emphasize that all critical fields depend on ξ , whereas H_c and H_{c1} are in addition functions of λ_L . The three critical fields, expressed as functions of the Ginzburg-Landau parameter, have to coincide at $\kappa = 1/\sqrt{2}$; this important physical condition is satisfied by the present approach.

B. Exploration of the superconducting critical field data

Figure 1(d) shows the upper critical fields H_{c2} , which are of key technological importance, for all materials that are predicted as Type-II superconductors in our database, systematically ranked in a $(T_c, 1/v_F)$ scatter plot. The blue-yellow background helps to structure the data by visualizing a BCS approximation for the upper critical fields:

$$H_{c2}^{\text{BCS}}(T_c, v_F) = \frac{\pi^2}{2e\hbar} \frac{(1.764 k_B T_c)^2}{v_F^2}. \quad (12)$$

In contrast, the point colors reflect the actual upper critical fields H_{c2} based on the Eliashberg gaps, which exceed H_{c2}^{BCS} due to the strong-coupling corrections discussed in more detail below. The plot shows how a material may attain a high H_{c2} : Either by exhibiting a high T_c (i.e., large Δ) or a low Fermi velocity, which both influence H_{c2} quadratically via the coherence length ξ . Interestingly, we find that some materials successfully balance both quantities, compensating for a slightly lower T_c by a higher inverse Fermi velocity. It can also be seen that the higher H_{c2} ranks are increasingly sparsely populated. Notably, several putative higher- T_c materials in the dataset, such as PdH, KB₆, RbB₆ and LiPdH₂, are *not* among the top- H_{c2} compounds.

The consistent dataset permits a series of new and unique perspectives on the magnetic response of conventional superconductors. In Fig. 2, we plot H_c , H_{c1} , and H_{c2} as a function of the predicted Ginzburg-Landau parameter κ , focusing on materials with $T_c > 1$ K. We find that the critical fields span four orders of magnitude, considerably exceeding the range of the corresponding T_c (1-37 K). At the boundary between Type-I and Type-II superconductivity ($\kappa = 1/\sqrt{2}$), one can see how H_{c1} and H_{c2} merge into H_c . We find that Type-II superconductors reach critical fields that exceed those of Type-I materials by several orders of magnitude (note the logarithmic scale): While Type-I superconductors attain at most $H_c \sim 0.24$ T here, upper critical fields of $H_{c2} > 66$ T can be observed among the Type-II superconductors. Comitantly, H_{c1} ranges between $\sim 10^{-2}$ and 3×10^{-1} T.

We observe that all high- H_{c2} materials are characterized by a relatively low average Fermi velocity v_F (represented by dark-purple squares). Notably, although $1/v_F$ correlates with the density of states at the Fermi energy $n(E_F)$ (red diamonds) with a Pearson coefficient of 0.66, there are several counterexamples such as LiTcN₂. Hence, v_F and $n(E_F)$ should be considered as individual quantities. Intriguingly, this implies that a high $n(E_F)$, while often beneficial for T_c , is *not* a sufficient indicator for a high critical magnetic field.

Figure 3(a) shows that Type-II superconductors exhibit, in addition to higher critical fields, a general trend towards higher T_c than Type-I superconductors. However, neither a large T_c nor a strong electron-phonon coupling λ are a guarantee for a high critical field [Fig. 1(d)]. This demonstrates that the critical magnetic fields are considerably more complex quantities than the critical temperatures, which renders them even more challenging to predict.

We find that the strong-coupling corrections to the superconducting gap as obtained from Eliashberg theory signifi-

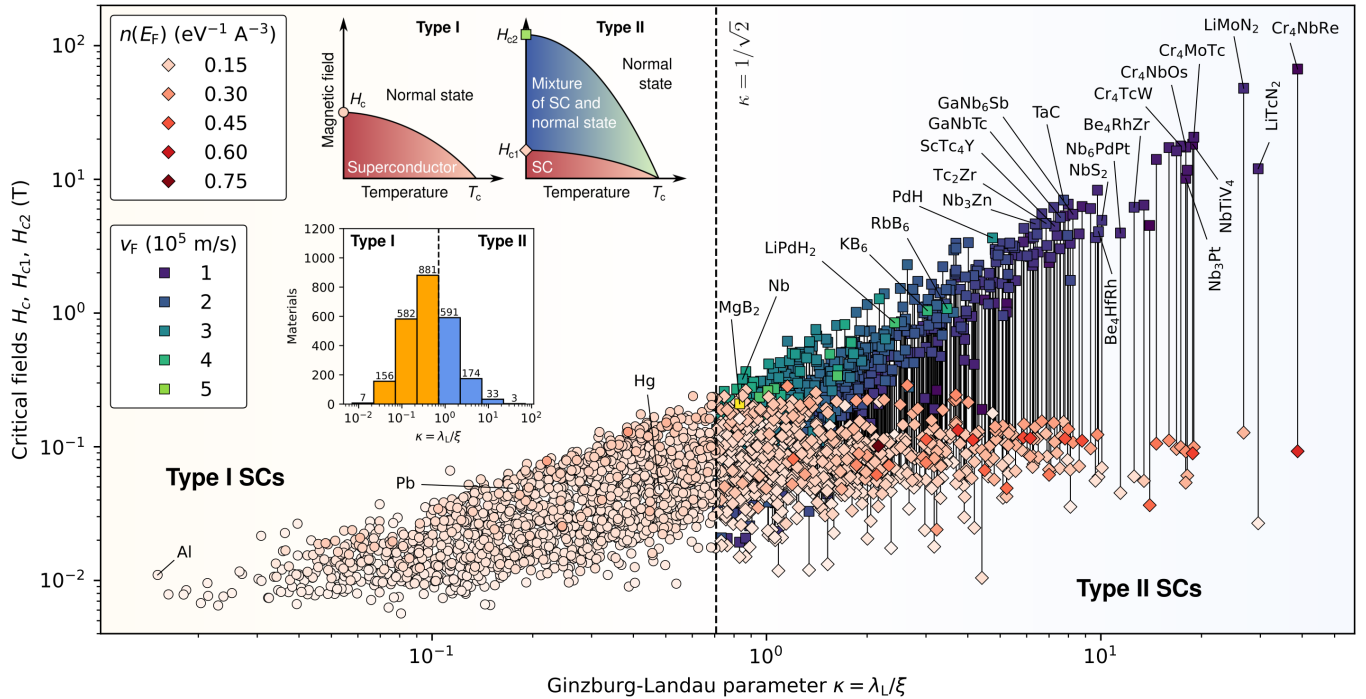


Figure 2. **Critical fields as a function of the Ginzburg-Landau parameter κ .** Type-I critical fields (left) are represented by a single point per material. For Type-II superconductors (right), upper and lower critical fields are represented by a square-diamond pair, respectively, connected by a vertical line. Red colors encode the electron-phonon renormalized density of states at the Fermi level $n(E_F)$, which is particularly relevant for H_c and H_{c1} . Green-purple colors represent the electron-phonon renormalized Fermi velocity v_F . Selected materials are labeled for reference. The histogram visualizes the distribution of κ and thus the number of Type-I versus Type-II superconductors. The figure focuses on materials with $T_c > 1$ K. All properties have been predicted consistently from DFT.

ciently enhance the predicted critical fields over a simple BCS approach. To illustrate this, the inset of Fig. 3(b) compares the Eliashberg gaps to the weak-coupling limit:

$$\Delta_{\text{BCS}}(0) = 1.764 k_B T_c. \quad (13)$$

For the paradigmatic strong-coupling superconductor Pb, we obtain a +17% increase of the gap, in good agreement with the literature [47], and thus of $H_c \sim \Delta$. For Type-II superconductors, this effect is even more pronounced and $H_{c2} \sim \Delta^2$ is enhanced by +37% for Nb and by +131% for La₃Tl. Intriguingly, the distribution of gap ratios $\Delta(0)/k_B T_c$ presents a clear maximum at the BCS reference and simultaneously shows a substantially extended tail with exponential decay reaching up to 3.55, which is more than twice the BCS value. To our knowledge, this is the first time that such a systematic statistical analysis of the Eliashberg strong-coupling corrections is discussed for a large set of realistic materials.

It is a common belief that there exist far more Type-II than Type-I superconductors. This prevailing impression in the community may be strongly shaped by high- T_c and unconventional superconductors, such as cuprates, Fe-based superconductors, and heavy-fermion systems. On the other hand, Roberts reported already in 1976 far more Type-II than Type-I superconductors [48] – long before the advent of unconventional superconductivity. Surprisingly, our findings stand in sharp contrast to this expectation: We observe a larger number

of Type-I than Type-II superconductors in our dataset, even if we focus exclusively on compounds with $T_c > 1$ K (1626 versus 801 materials; Fig. 2). We deduce several insights from this observation. First, our analysis pertains to the clean limit: Impurities and microstructural disorder, ubiquitous in real materials, tend to reduce the coherence length ξ and increase the London penetration depth λ_L , thereby driving nominally Type-I compounds towards Type-II behavior. The observed predominance of Type-I superconductivity thus emerges naturally within a clean-limit framework and demonstrates that our approach has the potential to uncover heretofore unrecognized systematic trends in superconducting materials.

Second, we examine the additional possibility that the surprising number of Type-I materials may be related to the restriction of our database to materials with smaller unit cells. In Fig. 3(c), we analyze whether the predicted Ginzburg-Landau parameter κ correlates with the number of atoms per unit cell, with the hypothesis that larger, more complex crystal structures may generically support higher critical fields. Intriguingly, the red linear regression line shows a clear positive trend, spanning an order of magnitude from $\kappa = 0.2$ to 2 as the number of atoms increases from 1 to 10. Figure 3(d) uncovers a similar correlation directly for the critical fields H_c and H_{c2} . These results provide a statistical confirmation of our hypothesis for a dataset of realistic materials and suggest that extending it to larger crystal structures in the future

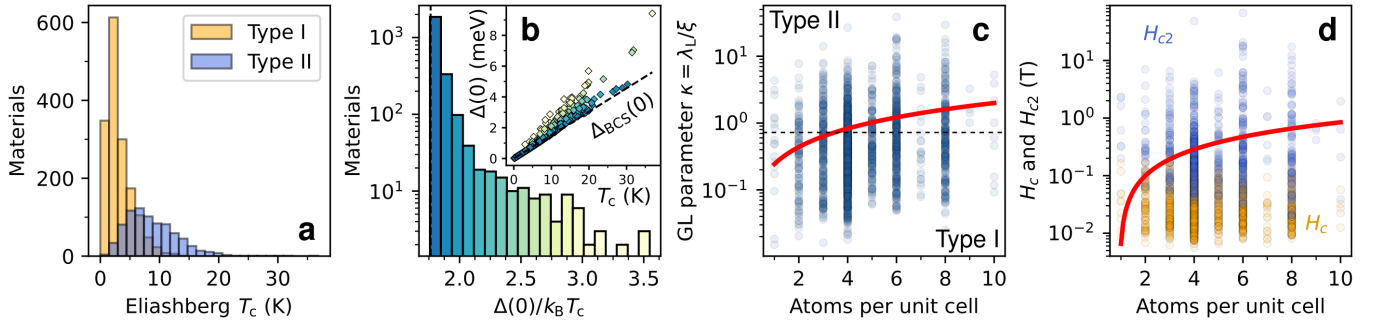


Figure 3. Statistical analysis of the superconducting properties. **a** Distribution of T_c for Type-I versus Type-II superconductors. **b** The distribution of $\Delta(0)/k_B T_c$ shows a clear maximum near the BCS reference, yet concomitantly a substantially extended tail reaching up to twice that value. The inset displays the Eliashberg superconducting gaps (diamonds) versus T_c , colored by $\Delta(0)/k_B T_c$. Comparison with the BCS expression (dashed line) highlights the strong-coupling corrections to the gaps. **c** Correlation of the Ginzburg-Landau parameter κ with the unit-cell size. **d** Correlation of the combined H_c (orange; Type I) and H_{c2} (blue; Type II) data with the unit-cell size. The linear regression lines are shown in red. Panels **a**, **c**, and **d** focus on materials with $T_c > 1$ K.

will increase the number of Type-II superconductors significantly. These fundamental insights are particularly relevant for identifying novel high-performance superconductors with small unit cells and a three-dimensional electronic structure.

C. The highest critical field materials and the technologically relevant regime

Tables I and II list the top- H_{c2} Type-II superconductors in our database, distinguished by the constituent elements. All of them are found deep in the Type-II regime ($\kappa \gg 1/\sqrt{2}$). In Table I, the highest H_{c2} is observed for LiMoN₂ (48 T), whose short coherence length (2.62 nm) and R3m symmetry distinguish it sharply from the rest of the materials. A comparison between LiMoN₂ and LiTcN₂ shows that electron doping alters the space group, nearly doubles ξ , and thus suppresses H_{c2} by a factor of four; yet at similar κ due to the enhanced λ_L . Interestingly, we find several Nb-based compounds in this list that crystallize in cubic, tetragonal, and hexagonal space

groups. In particular, Nb₃Pt (Pm $\bar{3}$ n) stands out due to a predicted $T_c \sim 13$ K and a strong $H_{c2} \sim 10$ T.

In Table II, which focuses specifically on materials that include Cr, Mn, V, and Ti, the upper critical fields reach even higher values. We observe many Cr-based compounds in this list, which are characterized by low Fermi velocities (see Figs. 1 and 2). The highest H_{c2} values are found in F43m-type compounds, most notably Cr₄NbRe, which reaches an exceptionally large $H_{c2} \sim 67$ T. Within this structural family, substitutions that increase the coherence length systematically suppress H_{c2} , as seen when moving from Cr₄NbRe ($\xi = 2.22$ nm) to compounds such as Cr₄MoTc and Cr₄TcW ($\xi \sim 4$ nm) or Cr₄TaW ($\xi = 7.37$ nm).

Although phases with non-zero magnetic moments were removed from the $\alpha^2 F(\omega)$ databases [27, 38], we speculate that some of these compounds may host subtle antiferromagnetic instabilities. However, Cr₃Ru is an experimentally established superconductor with $H_{c2} \sim 5$ T [49], and the prominence of related materials among the predicted high-critical-field compounds points to a potentially important trend. We therefore

Table I. Superconducting parameters (predicted) for the top- H_{c2} Type-II compounds that do not include Cr, Mn, V, and Ti.

Material	Spcgrp.	T_c^{El} (K)	λ_L (nm)	ξ (nm)	κ	H_{c1} (T)	H_{c2} (T)
LiMoN ₂	R3m	36.8	70.0	2.62	26.7	0.128	48.0
LiTcN ₂	I42d	23.0	154.7	5.24	29.5	0.027	12.0
Nb ₃ Pt	Pm $\bar{3}$ n	13.0	102.0	5.69	17.9	0.054	10.2
TaC	P6m2	23.8	53.1	6.86	7.7	0.153	7.0
Be ₄ RhZr	F43m	20.7	91.8	7.30	12.6	0.060	6.2
GaNb ₆ Sb	Pm $\bar{3}$	14.6	63.9	7.75	8.3	0.108	5.5
GaNbTc	I4mm	15.4	60.2	7.96	7.6	0.118	5.2
NbS ₂	P6 ₃ /mmc	16.1	82.2	8.16	10.1	0.070	4.9
Tc ₂ Zr	Fd3m	15.3	57.5	8.38	6.9	0.125	4.7
Nb ₃ Zn	Pm $\bar{3}$ n	15.1	53.5	8.41	6.4	0.141	4.6
ScTc ₄ Y	F43m	12.8	62.4	8.58	7.3	0.109	4.5
Be ₄ HfRh	F43m	19.2	88.6	9.00	9.8	0.060	4.1
Nb ₆ PdPt	Pm $\bar{3}$	12.7	104.2	9.11	11.4	0.045	4.0
La ₃ Tl	Pm $\bar{3}$ m	8.4	79.0	9.17	8.6	0.072	3.9
Mo ₃ Os	Pm $\bar{3}$ n	14.7	59.3	9.19	6.4	0.115	3.9

Table II. Superconducting parameters (predicted) for the top- H_{c2} Type-II compounds that include Cr, Mn, V, and Ti.

Material	Spcgrp.	T_c^{El} (K)	λ_L (nm)	ξ (nm)	κ	H_{c1} (T)	H_{c2} (T)
Cr ₄ NbRe	F43m	19.9	86.0	2.22	38.8	0.093	66.9
Cr ₄ MoTc	F43m	19.9	75.7	3.99	19.0	0.099	20.7
Nb ₂ TiV ₄	F43m	15.9	79.8	4.24	18.8	0.089	18.3
Cr ₄ TcW	F43m	19.6	74.7	4.30	17.3	0.100	17.8
Cr ₄ NbOs	F43m	18.5	78.0	4.35	18.0	0.092	17.4
Cr ₃ Ru	Pm $\bar{3}$ n	18.9	69.8	4.36	16.0	0.111	17.3
Cr ₄ ReW	F43m	19.4	75.6	4.49	16.8	0.096	16.3
Cr ₄ OsTa	F43m	17.5	70.8	4.83	14.7	0.105	14.1
Cr ₄ NbW	P1	17.8	96.2	5.30	18.1	0.061	11.7
Cr ₃ Os	Pm $\bar{3}$ n	18.1	61.5	6.30	9.8	0.123	8.3
Ti ₂ W	I4/mmm	15.3	56.7	7.10	8.0	0.135	6.5
Nb ₃ Sn ₂ Ti ₃	R32	13.7	96.3	7.16	13.5	0.056	6.4
Mn ₄ MoV	F43m	16.0	63.7	7.25	8.8	0.111	6.3
HfTi ₃ H	Pm $\bar{3}$ m	17.6	52.8	7.31	7.2	0.151	6.2
Cr ₄ TaW	F43m	17.4	68.7	7.37	9.3	0.097	6.1

list them separately, along with additional systems for which spin fluctuations may play a role.

Intriguingly, already within the first dataset presented here, we identify several promising candidates in or near the stringent technologically relevant regime, which we defined above by $T_c \gtrsim 20$ K and $H_{c2} \gtrsim 10$ T. Specifically, this comprises many of the Cr-based F43m materials listed in Tables II, particularly Cr₄NbRe, but also LiMoN₂, LiTcN₂, and particularly several Nb-based compounds from Table I including the well-known superconductor Nb₃Pt. A figure showing H_{c1} and H_{c2} as functions of T_c is provided in the Supplemental Information.

D. Comparison of predicted and experimental critical fields and key role of electron-phonon renormalizations

Finally, we assess the accuracy of our workflow by comparing the predicted superconducting parameters to experimental measurements. First, we analyze the Type classification based on the calculated κ [Fig. 4(a)]. Intriguingly, the predicted classification agrees with experiment for most materials in our representative test set, which comprises elemental superconductors, a number of A15 compounds, BiPb, and the layered superconductor MgB₂. As prominent examples, Pb is correctly predicted as Type I, and Nb and MgB₂ are correctly identified as Type II. We find MgB₂ close to the threshold, which may be rather conservative due to the underpredicted T_c (see below). Considering that all quantities are obtained exclusively from DFT, this accuracy is still remarkable.

Second, we compare predicted versus experimental critical fields H_c (Type I) and H_{c2} (Type II) quantitatively over four orders of magnitude [Fig. 4(b)]. The range given for the experimental values reflects their spread in the literature. We find that the agreement ranges from very good (Pb, Nb) to within an order of magnitude (MgB₂). We identify a central error source to be T_c , particularly for H_{c2} , where any T_c deviation propagates quadratically. An example is V, where spin fluctuations are expected to play a substantial role. If we rescale the critical fields to the experimental T_c , we achieve an improved agreement for several additional materials. Since the electronic properties are predicted rather accurately, even across different exchange-correlation functionals (see Methods), additional uncertainties remain significantly smaller than those introduced by T_c itself.

One of our most important findings is that a simple BCS approach is not sufficient: In addition to strong-coupling corrections to the superconducting gap, electron-phonon renormalizations of the effective mass are key to obtaining the correct order of magnitude for the critical fields. For Nb, we observe an enhancement of the predicted London penetration depth from $\lambda_L = 19$ to 27 nm (experiment: ~ 39 nm [54]) if considering electron-phonon renormalizations. At the same time, the predicted coherence length, evaluated by using the Eliashberg gap, decreases from $\xi = 68$ to 32 nm (experiment: ~ 38 nm). As a result, the Ginzburg-Landau parameter increases from $\kappa = 0.28$ to 0.85, bringing it much closer to the experimental value of ~ 1.03 and changing the theoreti-

cal classification of Nb from a Type-I to a Type-II superconductor, in agreement with experiment. A similar behavior is found for Pb, where λ_L increases from 20 to 29 nm (experiment: ~ 37 nm [54]), while ξ is reduced from 339 to 165 nm (experiment: ~ 83 nm). Consequently, the Ginzburg-Landau parameter is enhanced from $\kappa = 0.06$ to 0.17 (experiment: ~ 0.45). In both materials, the calculated λ_L remains systematically smaller than the experimental values, as expected. This leads to an underestimation of κ , yet significantly less severe than in the unrenormalized case. Ultimately, the predicted upper critical field H_{c2} of Nb is enhanced from 0.072 to 0.321 T (experiment: 0.2–0.8 T [48, 50, 51]) due to renormalization effects; similarly, the predicted H_c of Pb increases from 0.034 to 0.049 T (experiment: 0.08 T).

While the critical-field prediction is convincingly accurate for several Type-I and Type-II superconductors such as Al, Pb, Hg, Nb, Nb₃Pt, and also many hcp metals (Fig. 4), MgB₂ emerges as interesting challenge, which highlights both the complexity of its physics from the critical-field perspective as well as opportunities for future methodological innovation. The predicted T_c using the present workflow is half of the experimental value, similar to earlier work [55]. If we correct the upper critical field by using the experimental T_c , we obtain an enhancement from ~ 0.2 to ~ 0.8 T, which still deviates significantly from the experimental range of 3 T (*c* axis) to 14 T (*ab* plane) [53]. Possible reasons are the anisotropy and multiband nature of this material [32, 33]. In addition to anisotropic Fermi velocity components, the electron-phonon interactions and the resulting effective-mass renormalizations are expected to vary between different directions and different sheets of the Fermi surface. We speculate that accounting for these effects will considerably enhance the predictions for strongly anisotropic materials.

III. DISCUSSION

In this work, we have taken a first step towards the discovery of superconductors with high critical magnetic fields by developing a high-throughput workflow that combines clean-limit Eliashberg theory with density functional theory. By applying this framework to more than 7,300 electron-phonon-paired superconductors across diverse materials classes, we constructed a consistent database of critical fields H_c , H_{c1} , and H_{c2} together with the underlying electronic and superconducting properties. This unified perspective reveals previously unrecognized statistical trends in superconducting magnetic response: We uncovered an unexpectedly large number of Type-I superconductors and showed that larger and more complex crystal structures generically support higher critical fields and Type-II behavior. Moreover, we pointed out the importance of strong-coupling corrections and electron-phonon renormalizations of the effective mass for predictions of critical fields. In stark contrast, a simple BCS approach proved to be insufficient.

The resulting dataset comprises accurately sampled Fermi surfaces, averaged Fermi velocities, densities of states, Eliashberg critical temperatures and superconducting gaps, coher-

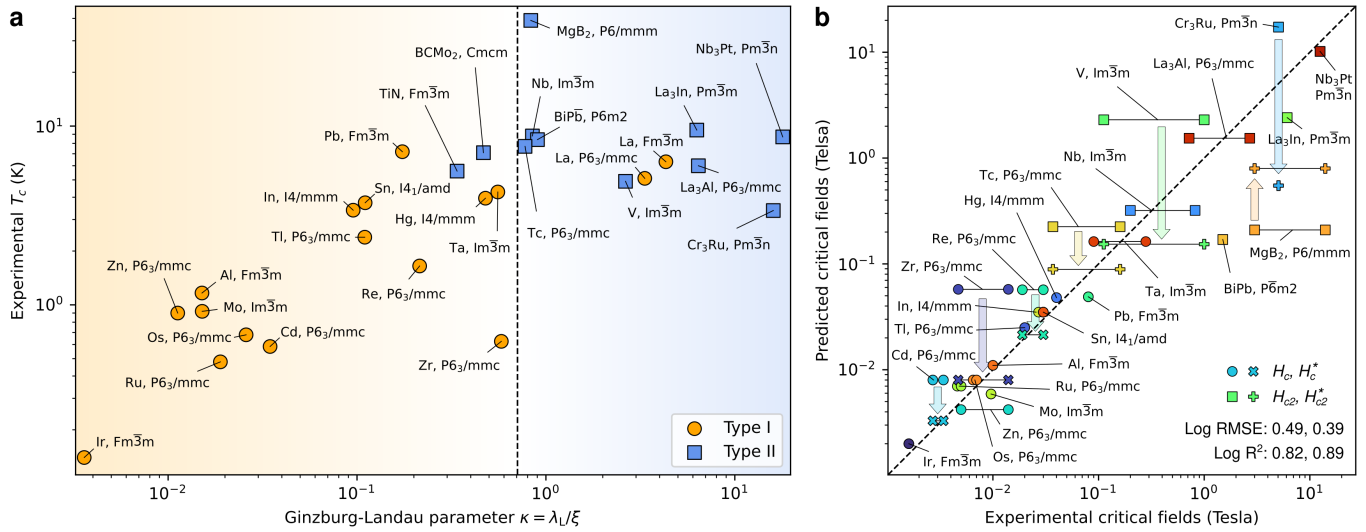


Figure 4. Comparison of predicted and experimental critical field properties. **a** Analysis of the Type-I (orange) versus Type-II (blue) superconductor classification, based on the Ginzburg-Landau parameter κ predicted entirely from first principles. The vertical axis corresponds to the experimental T_c , which shows that the classification cannot be trivially deduced from the critical temperature. **b** Parity plot of predicted versus experimental critical fields (H_c : circles; H_{c2} : squares). A table of the data, compiled from Refs. [48–53], is provided in the Supplemental Information. For those materials where the predicted T_c is in significant disagreement with the experimental value, we show in addition a rescaled critical field value using the experimental T_c (H_c^* : crosses; H_{c2}^* : pluses), which generally enhances the quantitative agreement as evidenced by the log RMSE and R^2 metrics.

ence lengths, London penetration depths, Ginzburg-Landau parameters, and critical magnetic fields. As such, it naturally complements existing first-principles databases that provide optimized crystal structures and Eliashberg spectral functions, extending them to magnetic-field-related superconducting properties that have so far remained unexplored at scale.

Beyond its fundamental significance, the present framework has direct technological relevance. The data allow access to the superheating field, a key quantity for minimizing power losses in superconducting RF cavities, and highlight materials with high critical fields that are of interest for compact and efficient electron-beam lithography systems in the semiconductor industry and for high-performance superconducting magnets for high-field laboratories, fusion reactors, particle accelerators, and MRI machines. More broadly, the insights obtained here are relevant for identifying high-performance superconductors with small unit cells and three-dimensional electronic structure.

Finally, by establishing a quantitative link between electronic structure, pairing, and magnetic response across a large materials space, this work lays the foundation for future AI-driven approaches to inverse materials design, enabling the targeted discovery of superconductors with simultaneously enhanced critical temperatures and critical magnetic fields.

IV. METHODS

For each of the $\sim 7,300$ compounds in the database, we performed an independent DFT structural optimization using the VASP code [41–43] in conjunction with the PBEsol

exchange-correlation functional [56] to confirm earlier findings, followed by a self-consistent and a non-self-consistent calculation to obtain accurate Fermi surfaces and densities of states. We use dense k -point grids that are scaled with the size of the unit cell (i.e., keeping a fixed density of k points). For example, we employ $40 \times 40 \times 35$ for MgB_2 and $45 \times 45 \times 45$ for Nb , which are further interpolated on a five times denser k -point grid before Fermi surface plotting and Fermi velocity evaluation using a modified version of the iFERMI code. We found this density to balance accuracy and feasibility in our high-throughput strategy. Materials from the earlier databases that we identified here to exhibit a band gap have been removed.

From extensive convergence tests for a subset of over 6,400 compounds from our database, we conclude that the k -grid convergence achieved by our methodology is statistically (i.e., considering the standard deviation) within $\sim \pm 2\%$ for $n(E_F)$ and $\sim \pm 1\%$ for v_F , which is considerably more accurate than typical T_c predictions. Moreover, for a test set of 17 elemental metals, we reproduce earlier v_F DFT predictions [57] within $\sim \pm 1\%$. Moreover, we found that the statistical variations of the predicted v_F between the exchange-correlation functionals LDA, PBE, and PBEsol are within $\sim \pm 3\%$.

We used the EPW code [39, 40], embedded in a high-throughput framework we developed in PYTHON, to solve the isotropic Eliashberg equations [36, 37] for the $\sim 7,300$ electron-phonon superconductors, which are characterized by

their Eliashberg spectral function $\alpha^2 F(\omega)$:

$$Z(i\omega_n) = 1 + \frac{\pi T}{\omega_n} \sum_{m=-\infty}^{\infty} \frac{\lambda_{n,m} \omega_m}{\sqrt{\omega_m^2 + \Delta^2(i\omega_m)}}, \quad (14)$$

$$Z(i\omega_n) \Delta(i\omega_n) = \pi T \sum_{m=-\infty}^{\infty} \dots \quad (15)$$

$$\dots \frac{[\lambda_{n,m} - \mu_{\text{EI}}^* \Theta(\omega_c - |\omega_m|)] \Delta(i\omega_m)}{\sqrt{\omega_m^2 + \Delta^2(i\omega_m)}}, \quad (16)$$

where

$$\lambda_{n,m} = 2 \int_0^\infty d\omega \frac{\omega \alpha^2 F(\omega)}{\omega^2 + (\omega_n - \omega_m)^2}, \quad (17)$$

$$i\omega_n = i(2n+1)\pi T \quad (n \in \mathbb{Z}). \quad (18)$$

Here we determine the Coulomb parameter μ_{EI}^* dynamically for each material and rescale it appropriately using a strategy motivated by Pellegrini and Sanna [12] and earlier considerations by Allen and Dynes [58]:

$$\frac{1}{\mu_{\text{EI}}^*} = \frac{1}{\mu_{\text{AD}}^*} + \ln\left(\frac{\omega_{\text{ph}}}{\omega_c}\right), \quad (19)$$

in which ω_{ph} is the maximum frequency of the phonon spectrum and $\omega_c = 10\omega_2$ is the cutoff for the Matsubara frequencies used during solving the Eliashberg equations. In this expression, we set $\mu_{\text{AD}}^* = 0.14$ for materials containing transition metals and $\mu_{\text{AD}}^* = 0.10$ otherwise.

For materials where solving the Eliashberg equations did not converge, usually in the case of very low $T_c \ll 1$ K, we resort to Allen-Dynes T_c and/or BCS gaps, following the philosophy of predicting critical magnetic fields for as many materials as possible.

While there are individually tailored strategies for some compounds that render a T_c closer to experiment, e.g., by solving the anisotropic Eliashberg equations [32, 33], their applicability in a high-throughput approach is so far unclear.

Here, we report the high-throughput values obtained consistently for all materials.

V. ACKNOWLEDGMENTS

We thank A. Gurevich, D. Larbalestier, and R. Margine for helpful discussions. B.G., J.J.H., G.R.S., R.G.H., and P.J.H. acknowledge funding by Grant No. NSF-DMREF-2522891. B.G., R.G.H., and P.J.H. acknowledge computational resources provided by the University of Florida via the 'AI and Complex Computational Research' program. P.M.D. acknowledges support from the Laboratory Directed Research and Development Program of Oak Ridge National Laboratory, managed by UT-Battelle, LLC, for the US Department of Energy. Notice of Copyright: This manuscript has been authored by UT-Battelle, LLC, under contract DE-AC05-00OR22725 with the US Department of Energy (DOE). The publisher acknowledges the US government license to provide public access under the DOE Public Access Plan (<http://energy.gov/downloads/doe-public-access-plan>).

VI. AUTHOR CONTRIBUTIONS

B.G., P.M.D., R.G.H., and P.J.H. conceived the project and conceptualized the framework. B.G. performed the DFT and Eliashberg calculations, implemented the high-throughput workflows, constructed the database, and performed the data analysis and visualization. J.J.H. and G.R.S. contributed experimental insights on the predictions and helped compiling the experimental reference data. B.G. and P.J.H. wrote the manuscript. All authors discussed the results and contributed to revising and editing the manuscript.

COMPETING INTERESTS

The authors declare no competing interests.

VII. DATA AVAILABILITY

The critical field database is available at <https://github.com/henniggroup>.

[1] J. G. Bednorz and K. A. Müller, Possible high- T_c superconductivity in the Ba-La-Cu-O system, *Zeitschrift für Physik B Condensed Matter* **64**, 189 (1986).

[2] M. K. Wu, J. R. Ashburn, C. J. Torng, P. H. Hor, R. L. Meng, L. Gao, Z. J. Huang, Y. Q. Wang, and C. W. Chu, Superconductivity at 93 K in a new mixed-phase Y-Ba-Cu-O compound system at ambient pressure, *Phys. Rev. Lett.* **58**, 908 (1987).

[3] A. Schilling, M. Cantoni, J. D. Guo, and H. R. Ott, Superconductivity above 130 K in the Hg-Ba-Ca-Cu-O system, *Nature* **363**, 56 (1993).

[4] J. Nagamatsu, N. Nakagawa, T. Muranaka, Y. Zenitani, and J. Akimitsu, Superconductivity at 39 K in magnesium diboride, *Nature* **410**, 63 (2001).

[5] Y. Kamihara, T. Watanabe, M. Hirano, and H. Hosono, Iron-Based Layered Superconductor La[O_{1-x}F_x]FeAs ($x = 0.05$ – 0.12) with $T_c = 26$ K, *Journal of the American Chemical Society* **130**, 3296 (2008).

[6] G. R. Stewart, Superconductivity in iron compounds, *Rev. Mod. Phys.* **83**, 1589 (2011).

[7] Y. Cao, V. Fatemi, S. Fang, K. Watanabe, T. Taniguchi, E. Kaxiras, and P. Jarillo-Herrero, Unconventional superconductivity in magic-angle graphene superlattices, *Nature* **556**, 43 (2018).

[8] V. Kamysbayev, A. S. Filatov, H. Hu, X. Rui, F. Lagunas, D. Wang, R. F. Klie, and D. V. Talapin, Covalent surface modifications and superconductivity of two-dimensional metal carbide MXenes, *Science* **369**, 979 (2020).

[9] J. A. Flores-Livas, L. Boeri, A. Sanna, G. Profeta, R. Arita, and M. Eremets, A perspective on conventional high-temperature superconductors at high pressure: Methods and materials, *Physics Reports* **856**, 1 (2020).

[10] L. Boeri, R. Hennig, P. Hirschfeld, G. Profeta, A. Sanna, E. Zurek, W. E. Pickett, M. Amsler, R. Dias, M. I. Eremets, C. Heil, R. J. Hemley, H. Liu, Y. Ma, C. Pierleoni, A. N. Kolmogorov, N. Rybin, D. Novoselov, V. Anisimov, A. R. Oganov, C. J. Pickard, T. Bi, R. Arita, I. Errea, C. Pellegrini, R. Requist, E. K. U. Gross, E. R. Margine, S. R. Xie, Y. Quan, A. Hire, L. Fanfarillo, G. R. Stewart, J. J. Hamlin, V. Stanev, R. S. Gonnelli, E. Piatti, D. Romanin, D. Daghero, and R. Valenti, The 2021 room-temperature superconductivity roadmap, *Journal of Physics: Condensed Matter* **34**, 183002 (2022).

[11] A. Molodyk and D. C. Larbalestier, The prospects of high-temperature superconductors, *Science* **380**, 1220 (2023).

[12] C. Pellegrini and A. Sanna, Ab initio methods for superconductivity, *Nature Reviews Physics* **6**, 509 (2024).

[13] K. Gao, T. F. T. Cerqueira, A. Sanna, Y.-W. Fang, Đ. Dangić, I. Errea, H.-C. Wang, S. Botti, and M. A. L. Marques, The maximum T_c of conventional superconductors at ambient pressure, *Nature Communications* **16**, 8253 (2025).

[14] D. Duan, Y. Liu, F. Tian, D. Li, X. Huang, Z. Zhao, H. Yu, B. Liu, W. Tian, and T. Cui, Pressure-induced metallization of dense $(\text{H}_2\text{S})_2\text{H}_2$ with high- T_c superconductivity, *Sci. Rep.* **4**, 6968 (2014).

[15] A. P. Drozdov, M. I. Eremets, I. A. Troyan, V. Ksenofontov, and S. I. Shylin, Conventional superconductivity at 203 kelvin at high pressures in the sulfur hydride system, *Nature* **525**, 73 (2015).

[16] M. Somayazulu, M. Ahart, A. K. Mishra, Z. M. Geballe, M. Baldini, Y. Meng, V. V. Struzhkin, and R. J. Hemley, Evidence for superconductivity above 260 K in lanthanum superhydride at megabar pressures, *Phys. Rev. Lett.* **122**, 027001 (2019).

[17] J. A. Flores-Livas, L. Boeri, A. Sanna, G. Profeta, R. Arita, and M. Eremets, A Perspective on Conventional High-Temperature Superconductors at High Pressure: Methods and Materials, *arXiv:1905.06693* (2019).

[18] W. E. Pickett, Colloquium: Room temperature superconductivity: The roles of theory and materials design, *Rev. Mod. Phys.* **95**, 021001 (2023).

[19] V. Stanev, C. Oses, A. G. Kusne, E. Rodriguez, J. Paglione, S. Curtarolo, and I. Takeuchi, Machine learning modeling of superconducting critical temperature, *npj Computational Materials* **4**, 29 (2018).

[20] B. Meredig, E. Antono, C. Church, M. Hutchinson, J. Ling, S. Paradiso, B. Blaiszik, I. Foster, B. Gibbons, J. Hattrick-Simpers, A. Mehta, and L. Ward, Can machine learning identify the next high-temperature superconductor? Examining extrapolation performance for materials discovery, *Mol. Syst. Des. Eng.* **3**, 819 (2018).

[21] M. J. Hutzler, A. M. Shipley, and R. J. Needs, Predicting novel superconducting hydrides using machine learning approaches, *Phys. Rev. B* **101**, 144505 (2020).

[22] S. R. Xie, Y. Quan, A. C. Hire, B. Deng, J. M. DeStefano, I. Salinas, U. S. Shah, L. Fanfarillo, J. Lim, J. Kim, G. R. Stewart, J. J. Hamlin, P. J. Hirschfeld, and R. G. Hennig, Machine learning of superconducting critical temperature from eliashberg theory, *npj Computational Materials* **8**, 14 (2022).

[23] Z. Zhang, T. Cui, M. J. Hutzler, A. M. Shipley, H. Song, M. Du, V. Z. Kresin, D. Duan, C. J. Pickard, and Y. Yao, Design Principles for High-Temperature Superconductors with a Hydrogen-Based Alloy Backbone at Moderate Pressure, *Phys. Rev. Lett.* **128**, 047001 (2022).

[24] K. Choudhary and K. Garrity, Designing high- T_c superconductors with BCS-inspired screening, density functional theory, and deep-learning, *npj Computational Materials* **8**, 244 (2022).

[25] D. Wines, K. Choudhary, A. J. Biacchi, K. F. Garrity, and F. Tavazza, High-Throughput DFT-Based Discovery of Next Generation Two-Dimensional (2D) Superconductors, *Nano Letters* **23**, 969 (2023).

[26] T. Sommer, R. Willa, J. Schmalian, and P. Friederich, 3DSC - a dataset of superconductors including crystal structures, *Scientific Data* **10**, 816 (2023).

[27] J. B. Gibson, A. C. Hire, P. M. Dee, O. Barrera, B. Geisler, P. J. Hirschfeld, and R. G. Hennig, Accelerating superconductor discovery through tempered deep learning of the electron-phonon spectral function, *npj Computational Materials* **11**, 7 (2025).

[28] J. B. Gibson, A. C. Hire, P. Prakash, P. M. Dee, B. Geisler, J. S. Kim, Z. Li, J. J. Hamlin, G. R. Stewart, P. J. Hirschfeld, and R. G. Hennig, Developing a complete AI-accelerated workflow for superconductor discovery (2025), *arXiv:2503.20005* [cond-mat.supr-con].

[29] P. Prakash, J. B. Gibson, Z. Li, G. D. Gianluca, J. Esquivel, E. Fuemmeler, B. Geisler, J. S. Kim, A. Roitberg, E. B. Tadmor, M. Liu, S. Martiniani, G. R. Stewart, J. J. Hamlin, P. J. Hirschfeld, and R. G. Hennig, Guided diffusion for the discovery of new superconductors (2025), *arXiv:2509.25186* [cond-mat.supr-con].

[30] D. Larbalestier, A. Gurevich, D. M. Feldmann, and A. Polyaniskii, High- T_c superconducting materials for electric power applications, *Nature* **414**, 368 (2001).

[31] G. Blatter, M. V. Feigel'man, V. B. Geshkenbein, A. I. Larkin, and V. M. Vinokur, Vortices in high-temperature superconductors, *Rev. Mod. Phys.* **66**, 1125 (1994).

[32] H. J. Choi, D. Roundy, H. Sun, M. L. Cohen, and S. G. Louie, First-principles calculation of the superconducting transition in MgB_2 within the anisotropic Eliashberg formalism, *Phys. Rev. B* **66**, 020513 (2002).

[33] E. R. Margine and F. Giustino, Anisotropic Migdal-Eliashberg theory using Wannier functions, *Phys. Rev. B* **87**, 024505 (2013).

[34] National Academies of Sciences, Engineering, and Medicine, *The Current Status and Future Direction of High-Magnetic-Field Science and Technology in the United States* (The National Academies Press, Washington, DC, 2024).

[35] W. Kohn and L. J. Sham, Self-consistent equations including exchange and correlation effects, *Phys. Rev.* **140**, A1133 (1965).

[36] G. M. Eliashberg, Interaction between electrons and lattice vibrations in a superconductor, *Sov. Phys. JETP* **11**, 696 (1960).

[37] J. P. Carbotte, Properties of boson-exchange superconductors, *Rev. Mod. Phys.* **62**, 1027 (1990).

[38] T. F. T. Cerqueira, A. Sanna, and M. A. L. Marques, Sampling the materials space for conventional superconducting compounds, *Advanced Materials* **10.1002/adma.202307085** (2023).

[39] S. Poncé, E. Margine, C. Verdi, and F. Giustino, EPW: Electron-phonon coupling, transport and superconducting properties using maximally localized Wannier functions, *Computer Physics Communications* **209**, 116 (2016).

[40] F. Giustino, M. L. Cohen, and S. G. Louie, Electron-phonon interaction using Wannier functions, *Phys. Rev. B* **76**, 165108 (2007).

[41] G. Kresse and J. Furthmüller, Efficient iterative schemes for ab initio total-energy calculations using a plane-wave basis set, *Phys. Rev. B* **54**, 11169 (1996).

[42] G. Kresse and J. Furthmüller, Efficiency of ab-initio total energy calculations for metals and semiconductors using a plane-wave basis set, *Computational Materials Science* **6**, 15 (1996).

[43] G. Kresse and D. Joubert, From ultrasoft pseudopotentials to the projector augmented-wave method, *Phys. Rev. B* **59**, 1758 (1999).

[44] M. D. Whitmore and J. P. Carbotte, Effects of impurities on anisotropic superconductors with repulsive average interaction, *Journal of Physics F: Metal Physics* **11**, 2585 (1981).

[45] M. Tinkham, *Introduction to Superconductivity*, Dover Books on Physics Series (Dover Publications, 2004).

[46] E. H. Brandt, The vortex lattice in Type-II superconductors: Ideal or distorted, in bulk and films, *physica status solidi (b)* **248**, 2305 (2011).

[47] B. Mitrović, H. G. Zarate, and J. P. Carbotte, The ratio $2\Delta_0/k_B T_c$ within Eliashberg theory, *Phys. Rev. B* **29**, 184 (1984).

[48] B. W. Roberts, Survey of superconductive materials and critical evaluation of selected properties, *Journal of Physical and Chemical Reference Data* **5**, 581 (1976).

[49] Z. Zhu, Y.-J. Zhang, Y. Li, Q. Li, W. Duan, and H.-H. Wen, Comparative studies on superconductivity in Cr_3Ru compounds with bcc and A15 structures, *Journal of Physics: Condensed Matter* **34**, 475602 (2022).

[50] J. Eisenstein, Superconducting elements, *Rev. Mod. Phys.* **26**, 277 (1954).

[51] B. T. Matthias, T. H. Geballe, and V. B. Compton, Superconductivity, *Rev. Mod. Phys.* **35**, 1 (1963).

[52] K. Schwochau, *Techneum: Chemistry and Radiopharmaceutical Applications* (Wiley, 2000).

[53] M. Zehetmayer, M. Eisterer, J. Jun, S. M. Kazakov, J. Karpinski, A. Wisniewski, and H. W. Weber, Mixed-state properties of superconducting MgB_2 single crystals, *Phys. Rev. B* **66**, 052505 (2002).

[54] *Introduction to Solid State Physics, 7th Ed* (Wiley India Pvt. Limited, 2007).

[55] S. R. Xie, G. R. Stewart, J. J. Hamlin, P. J. Hirschfeld, and R. G. Hennig, Functional form of the superconducting critical temperature from machine learning, *Phys. Rev. B* **100**, 174513 (2019).

[56] J. P. Perdew, A. Ruzsinszky, G. I. Csonka, O. A. Vydrov, G. E. Scuseria, L. A. Constantin, X. Zhou, and K. Burke, Restoring the Density-Gradient Expansion for Exchange in Solids and Surfaces, *Phys. Rev. Lett.* **100**, 136406 (2008).

[57] D. Gall, Electron mean free path in elemental metals, *Journal of Applied Physics* **119**, 085101 (2016).

[58] P. B. Allen and R. C. Dynes, Transition temperature of strong-coupled superconductors reanalyzed, *Phys. Rev. B* **12**, 905 (1975).